SAND2020-2273C

High-Fidelity Modeling and Structural Analysis of an Additively Manufactured Component with Defects

Moheimin Khan, J. Justin Wilbanks, Brian C. Owens
Sandia National Laboratories[1]
P.O. Box 5800 – MS0840
Albuquerque, NM, 87185

ABSTRACT

Additive manufacturing (AM) offers several advantages over traditional methods but resulting parts can contain defects such as porosity and geometric irregularity. X-ray computed tomography (CT) scans are often used to identify these defects and validate against an ideal geometry. However, it is often difficult to determine the influence of defects on quality or performance. For structural components, AM defects can act as stress concentrations or reduce stiffness and mass. In this work, the presence of these defects is considered and the resulting effects on dynamic characteristics are quantified. A high-fidelity finite element (FE) model of the as-built AM part is generated using an overlay-grid hexahedral meshing scheme. In addition, a simplified defect modeling approach is considered, and results are compared to the nominal case. Structural analysis is performed to determine the impact on acceleration response, stress response, and other quantities of interest. Utilizing the component CT scan data to generate an FE model can provide improved accuracy in predicting dynamic properties and performing failure assessment.

INTRODUCTION

Metal Additive Manufacturing (AM) processes can be utilized to fabricate parts with complex geometries that are beyond the capabilities of traditional methods. AM components are excellent in structural applications and designs are often optimized in terms of weight and stiffness. However, quality is still a major concern since the AM process can introduce defects such as porosity and voids, surface roughness, cracks, and dimensional inaccuracy or distortion [1]. For structural components, the presence of such defects can result in stress concentrations and a reduction in stiffness and mass, which can adversely affect the dynamic characteristics. To properly assess the performance of a component under dynamic loading such as shock and vibration, it is important to quantify the influence of these defects.

X-ray Computed Tomography (CT) scanning is a non-destructive inspection method that is commonly employed to identify defects in AM parts. A detailed three-dimensional (3D) part representation is generated by reconstructing individual x-ray images taken from the scanning process. The data is typically used to determine the location and size of defects and compare against an ideal or nominal geometry [2]. Characterizing the defects in an AM part is necessary to ensure quality during manufacturing, but the inspection data has seen limited use in structural analysis. Some research has been done on incorporating CT scan data into models, such as the work by Esposito et al. [3], but the focus was on stress-strain behavior of tensile specimens.

This study evaluates the impact of AM defects on the dynamic behavior of a structural component by directly utilizing CT scan data in the analysis procedure. Finite element (FE) analysis is performed to compute natural frequencies, mode shapes, accelerations, and stresses for the AM component. A comparison is made to both the nominal case and a simplified defect model to assess the influence of the defects on structural response.

PART MANUFACTURE AND SCAN

The component evaluated in this study is a tube with a length of 95 mm, wall thickness of 1 mm, and a flange with four holes and an outer diameter of 120 mm. It was manufactured using a directed energy deposition (DED) technique, in which a stream of metal powder and inert gas is fed through a nozzle and consolidated by a laser to build up the part [4]. A cross section of the component highlighting one of the major defects on the inner wall is shown in Fig. 1.

AM Defect
Fig. 1- Component with Defect on Inner Wall

X-ray CT scans were carried out on the AM part and the data was reconstructed into a stereolithography (STL) file, which was subsequently used to generate the FE model. Some of the CT scan parameters include a minimum 70 μm resolution and a total of approximately 3000 projections. An image of the scan showing two different cross-sectional views is given in Fig. 2.
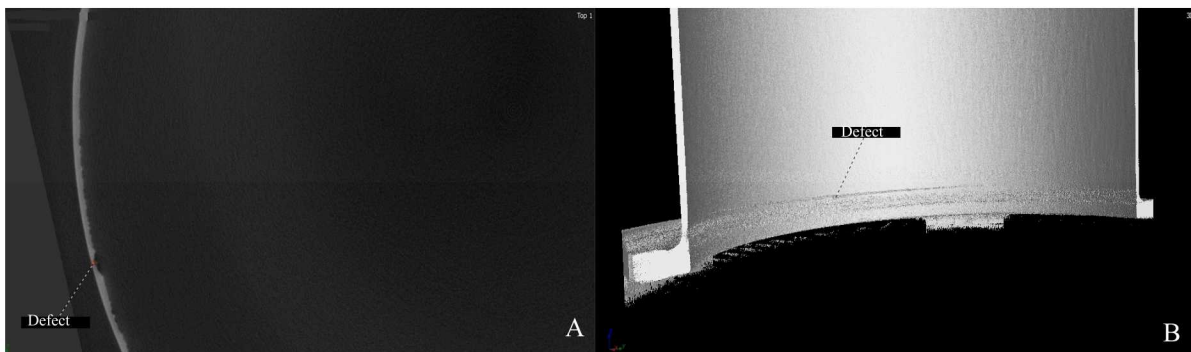

Fig. 2- CT Scan of Component with Transverse Cross Section at Defect (A) and Axial Cut-Away (B)

FE MODEL

Three different FE models of the component were generated using Sandia's CUBIT meshing software. The first uses the defect-free nominal geometry with dimensions from the CAD model, shown in Fig. 3. The second is the AM model, which contains defects and is based on the STL file of the as-built part. A close-up of the STL reconstructed from the CT scan is shown in Fig. 4. The third model is a simplified defect model which approximates major surface defects, such as the groove and voids at the inner wall of the tube and includes the variation in the dimensions of the flange. This simplified model was generated by starting with the nominal model, then removing groups of elements at the major defect locations identified from the scan. An image of one of the approximated surface defects is shown in Fig. 5. Other internal defects such as small voids and pores were not included in this model.
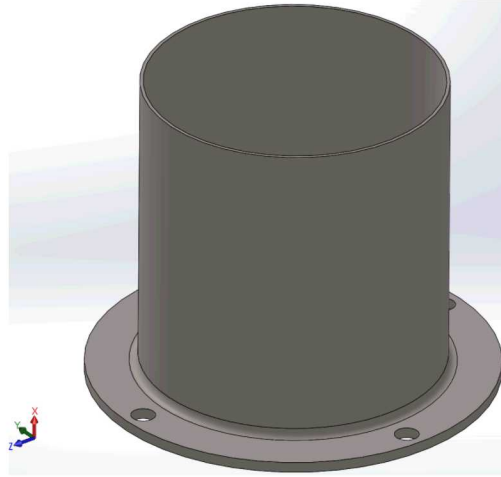

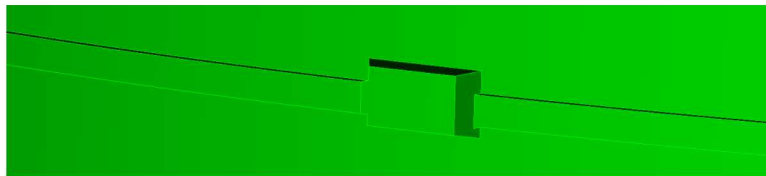Fig. 3- Component CAD Model

Fig. 4- STL Closeup

Fig. 5- Simplified Defect

The AM model was meshed with the SCULPT parallel algorithm, which uses a grid overlay scheme and volume fraction data from the STL file to construct a hexahedral mesh. SCULPT is suited for meshing complex geometry and performs well even with the irregular and discontinuous facets present in a reconstructed CT scan. The final mesh had a 0.15 mm average edge length and a total of 18 million linear hexahedral elements (approximately 20 million model nodes). The images in Fig. 6 and Fig. 7. emphasize the level of detail that is captured with the high-fidelity mesh. The voids and surface roughness present at the inner surface and outer flange are adequately

represented in the resulting model, and the refined mesh size can resolve many of the smaller internal pores that are distributed throughout the part.
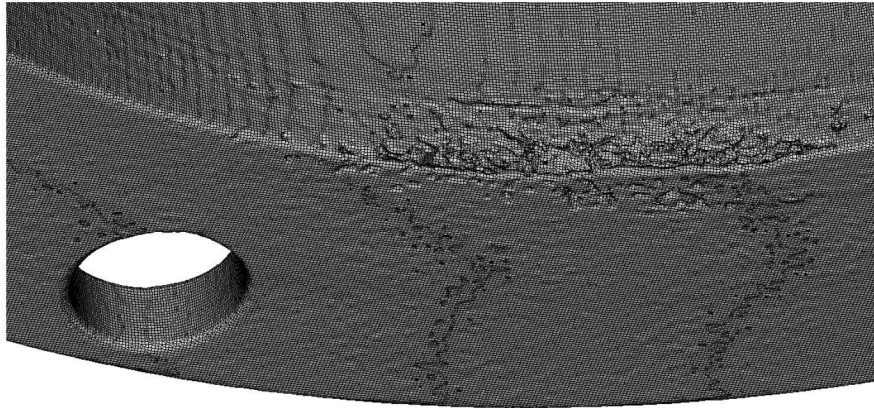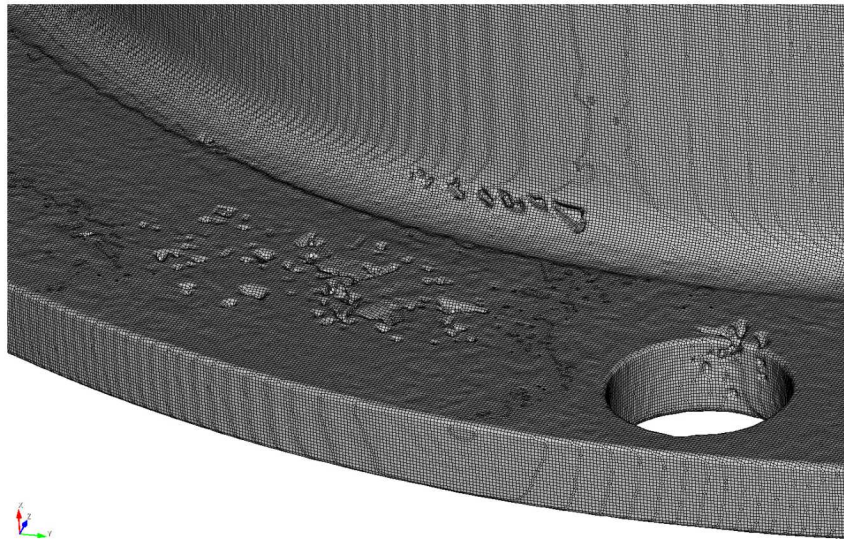

Fig. 6- AM Mesh Inner Surface

Fig. 7- AM Mesh Outer Surface

To clarify the large-scale differences between the geometry of the nominal and AM part, the meshes are shown overlaid in Fig. 8. Some notable discrepancies are that the cylindrical shape of the tube is distorted for the AM mesh, and the flange thickness, diameter, and fillet size are also different. These geometric distortions along with the smaller voids present throughout the AM model are the main defects of interest in the analysis and are expected to have the largest effect on the structural response of the part.
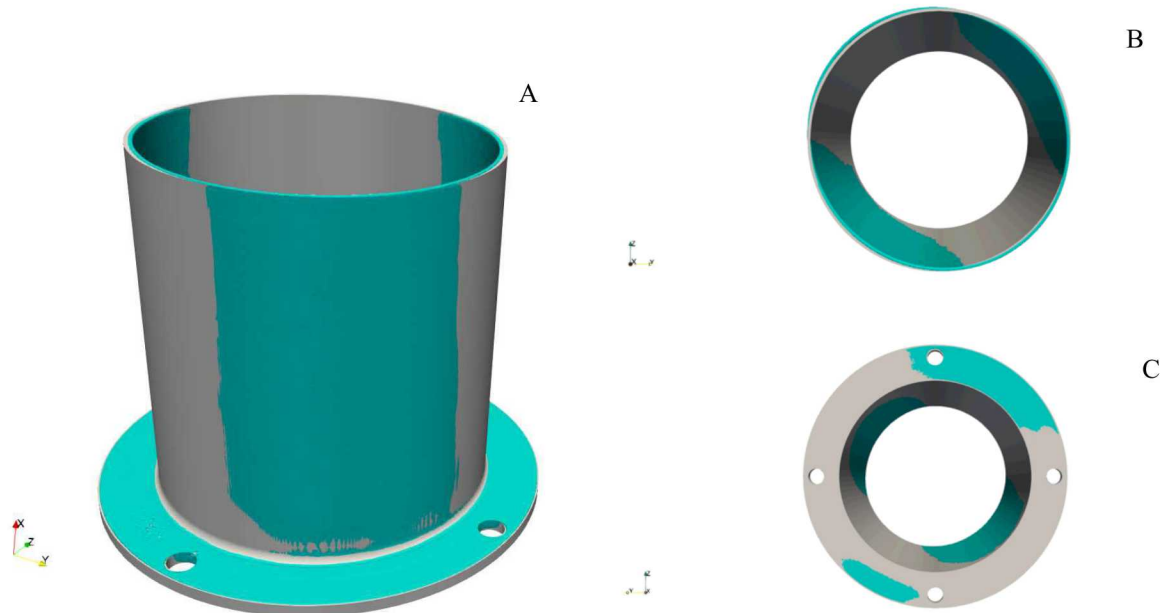
Fig. 8- Comparison of AM mesh in Cyan and Nominal in Gray; Isometric (A), Top (B), and Bottom (C) Views

ANALYSIS PROCEDURE

To perform the FE analysis on each of the models, Sandia's Sierra/SD code was utilized. Sierra/SD is a massively parallel, implicit, linear elastic structural dynamics code [5]. A modal analysis was performed for the component in the fixed base condition to obtain modes up to a frequency of 13 kHz, a total of 75 modes. The base of the flange was constrained at the hole locations using a seismic mass and rigid bar elements (RBARs), as shown in in Fig. 9. The fixed base modes between the models were compared using the modal assurance criterion (MAC).

Using the modal data, transient shock and random vibration analyses were performed. The inputs given in Fig. 10 are as follows: a 100 G Haversine pulse with 0.4 ms duration for the shock, and 0.1 G^2/Hz (26 GRMS) flat random vibration from 500 to 7500 Hz. In each case, a base acceleration was enforced at the seismic mass location. Axial (X) and transverse (Z) accelerations were applied in separate loading cases. The Y direction was also considered but the Z results are presented here due to presence of larger defects on that axis. Linear elastic and isotropic Ti6Al4V material properties were used for each case. In addition, a uniform modal damping value of 2% was chosen.
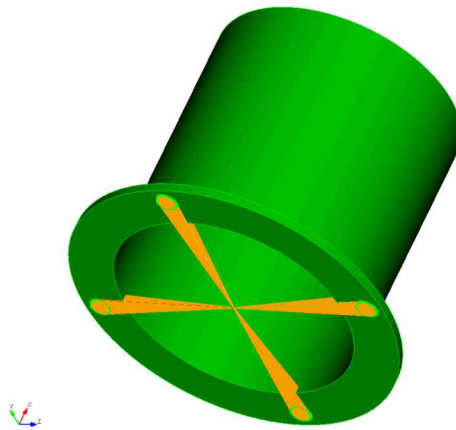

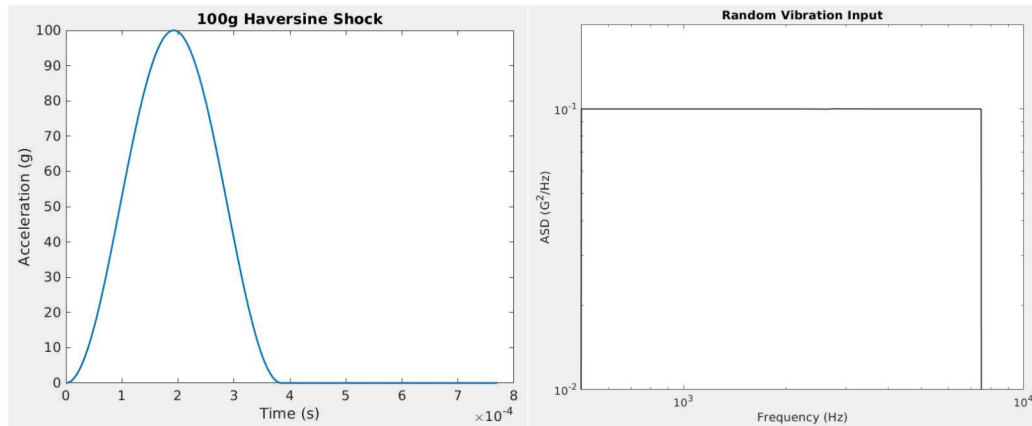Fig. 9- FE Model with Seismic Mass and RBARS for Fixed Base Condition

Fig. 10- Shock and Random Vibration Input Profiles

MODAL ANALYSIS RESULTS

Mode shapes and frequencies were calculated for the each of the three models (the nominal, AM, and simplified defect), and the nominal was used as a baseline for comparison. For reference, natural frequencies for the first 30 modes are tabulated in Table A 1 in the appendix along with percent differences for each case. Table 1 below shows the frequencies for 3 selected modes for each case. Modes 1, 4, and 7 are representative of the general trend that the AM model had lower frequencies and the simplified case showed little difference from the nominal.

Table 1- Modal Analysis Summary

Mode	Nominal Freq. (Hz)	AM Freq. (Hz)	Simplified Freq. (Hz)
1	730	681	737
4	1567	1406	1597
7	2697	2451	2754

Overall, the AM frequencies are up to about 10% lower than nominal, which is likely due to reduced stiffness of the component caused by the void defects present throughout the tube wall and at the flange fillet. Results also showed that the simplified model had similar dynamic properties as the nominal case, with the largest difference in frequency of only 3%. Thus, the surface defect representation was an oversimplification and did not appear to adequately capture the contribution of the actual defects present in the part. It is also important to note that the AM model had a slightly lower mass (under 5%) compared to the nominal case, so this was also a factor in the observed frequency shift.

To further quantify the difference in mode shapes, the MAC was calculated between the nominal and AM models. The MAC plot for 30 modes up to 8 kHz is presented in Fig. 11A. It shows good overall correlation, meaning that the defects did not significantly change most of the mode shapes. However, some specific modes do not have a high correlation, and two of these are discussed in detail.
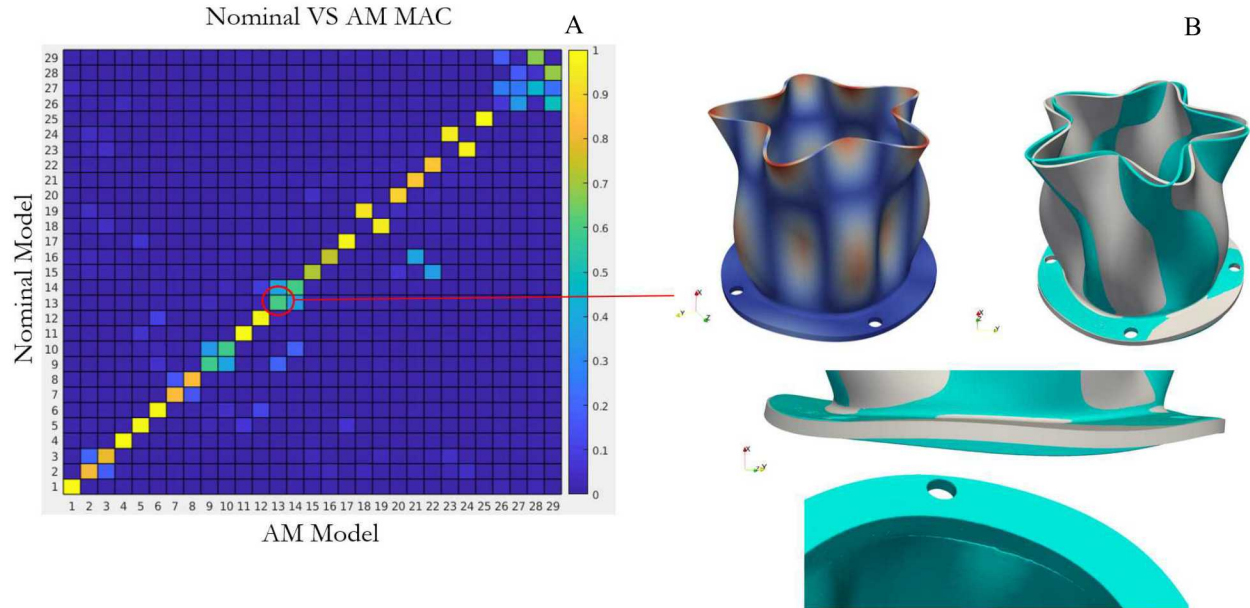
Fig. 11- MAC (A), and Overlay of Nominal (gray) and AM (cyan) Mode Shapes (B)

For mode 13, the nominal frequency is 4522 Hz compared to the AM value of 4353 Hz. The MAC value for these modes is 0.6. The difference can be seen in Fig. 11B, which shows the overlaid mode shapes to highlight the AM altered shape, especially at the flange location where one of the major defects is present.

Some of the higher frequency modes have even lower MAC values. Mode 26, shown in Fig. 12, is a new mode shape that is introduced in the AM model. It does not correspond exactly to any mode in the nominal case, which explains the low MAC of under 0.1. The closest matching modes are 27 and 29, illustrated in Fig. 12B. This mode shape unique to the AM model emphasizes that defects can have a large effect on the component dynamics.
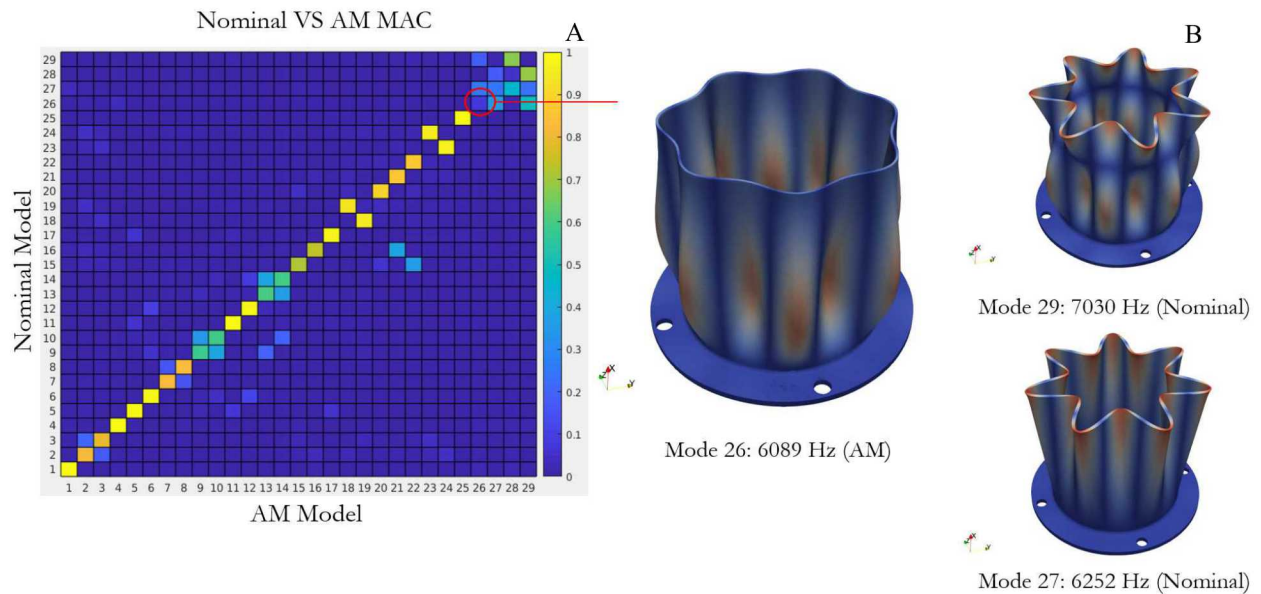

Mode 26: 6089 Hz (AM)

Mode 29: 7030 Hz (Nominal)

Mode 27: 6252 Hz (Nominal)

Fig. 12 MAC (A), and Nominal and AM Mesh Mode Shapes (B)

SHOCK ANALYSIS RESULTS

A 100 G, 0.4 ms duration Haversine pulse shown in Fig. 10 was applied to the component as a base acceleration. The 3 cartesian axes were analyzed independently and the peak shock response and acceleration values for each input are provided in Table A 2 for reference in the appendix. Results for the axial (X-axis) and transverse (Z-axis) directions are presented in this section.

For loading in the axial direction, Fig. 13 shows the shock response spectrum (SRS) for each model at the location of maximum response. The SRS includes the maxi-max absolute acceleration (MMAA) and 3% critical damping.
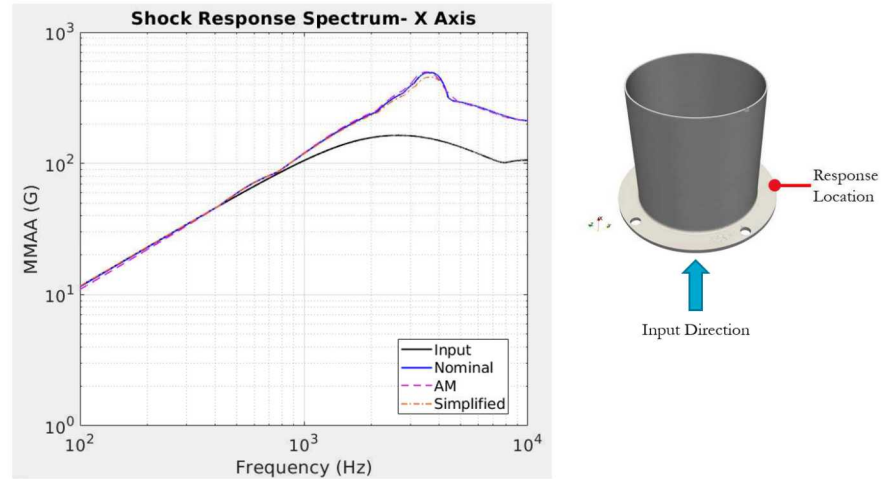

Fig. 13- Axial (X-Axis) Response and Location

The defects present in the component appear to have little effect on the shock response of the component since each model has approximately the same SRS profile. The maximum value of acceleration of 190 G is located at the flange near the hole for each case. The peak shock response is within 10 G at 4 kHz, but the values are slightly lower for the simplified defect case.

Although the axial shock response is similar for all three models, there are some larger changes for the transverse loading case. For input in the Z-direction, the peak transverse acceleration is located near the top of the tube, as shown in Fig. 14. Here, the peak shock response is about 30 G higher for the AM over the nominal, and the frequency shift in the AM model is more pronounced compared to the axial case. Still, the overall difference in acceleration response for both axes among the three models is minimal.
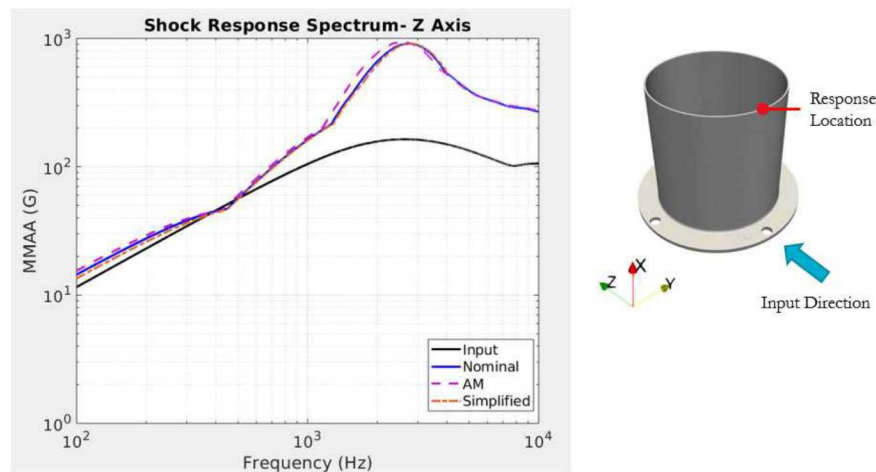

Fig. 14- Transverse (Z-Axis) Response and Location

In addition to the SRS, stresses were computed for each of the loading scenarios. Input in the transverse Z direction caused in the highest stress values, shown in Fig. 15. The stress contours provide the maximum von Mises stress in any given element across all analysis time steps. In Fig. 15A, a local stress concentration arises at the inner wall due to the groove defect, but the values are still over an order of magnitude below the yield strength of typical Ti6Al4V. In addition, Fig. 15B shows increased stress at the slightly reduced fillet radius of the AM, which was also seen in the random vibration analysis and will be discussed in detail later in that section.
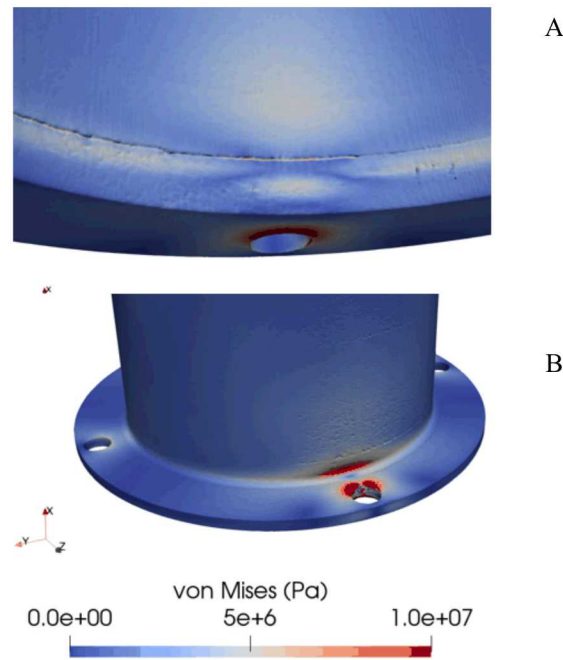

Fig. 15- Maximum von Mises Stress: Shock in Z-Direction, Inner Surface (A), and Outer Surface Near Flange (B)

RANDOM VIBRATION ANALYSIS RESULTS

As in the shock analysis, the random vibration input was applied to the base of the component via the seismic mass. Acceleration auto-spectral densities (ASD) are presented to show the response for each of the models over the 500 to 7500 Hz input band. A summary of the peak values for each direction are given in Table A 3 in the appendix.

Results for axial loading are shown in Fig. 16. In this loading case, there is a higher peak response for the AM model near 5 kHz compared to the nominal, and the frequency shift results in lower GRMS. The overall shape of the ASD curve is similar for all three cases, although the simplified model has about double the response at 5 kHz.
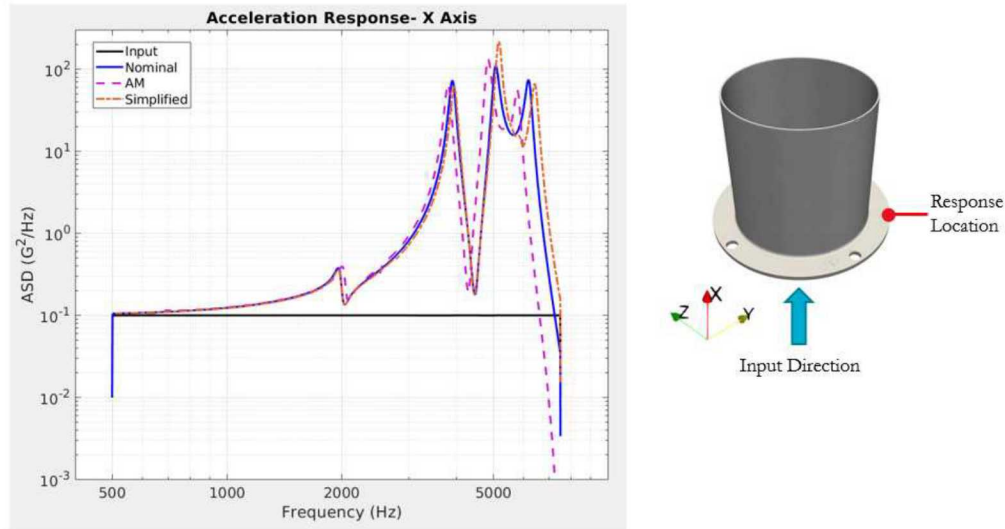
Fig. 16- Axial (X-Axis) Response and Location

The transverse analysis results further showcase the variation in response between the models. The ASD for the AM model is once again shifted to lower frequencies and has a higher peak response compared to the nominal at 2700 Hz. At 6 kHz, the response changes significantly, which is consistent with the presence of a new AM mode discussed earlier and shown in Fig. 12. Furthermore, like the axial loading case, the peak response near 5 kHz is much higher than the nominal version and the frequency shift of the contributing mode is approximately 5%. The overall profile for each ASD curve is similar, but the change in magnitude and frequency is larger than seen in the shock analysis, especially above 5 kHz where the different AM mode shapes significantly affect the peak response.

Fig. 17- Transverse (Z-Axis) Response and Location

Results from the random vibration analysis show that the AM model can have a much different acceleration response than the nominal model. In the transverse loading case, the unique AM mode shape had close to an order of magnitude difference in response to the input near 6 kHz. By generating a detailed model that includes defects, this effect on the component response can be accounted for. In cases where multiple AM parts are used in a complex assembly, even larger variability could be expected.

Stress results for the random vibration analysis are also presented for the transverse loading case. Fig. 18 shows the root mean square von Mises (VRMS) stress distribution for the part. The max 3σ VRMS stress in the tube fillet was about 18% higher for the AM case: 20 MPa vs 16.5 MPa. Similar to the shock analysis case, the stress values were

low compared to the material yield strength, but still showed a large relative difference. At the specific location illustrated in Fig. 18A, the higher stress results from reduced material volume at the fillet due to geometric distortions in the AM part, as mentioned in the FE model section. Fig. 18B shows the comparison to the nominal stress distribution. Here, stresses near the bolt hole location were ignored due to the high artificial stresses imposed by the RBAR constraints. A slight stress concentration at the simplified groove defect is also shown in Fig. 18C, but the VRMS magnitude is lower than the fillet region.

Stresses for the AM part are also highly concentrated at the void defects on the fillets, but those were not considered in the study. Since a linear elastic analysis was performed, no residual stress or lack of fusion in the AM processing was represented in the model. Although the stress analysis based on an elastic material model and yield failure criteria has its limits for AM parts, the analysis was still able to highlight some key points that would have been missed without a high-fidelity mesh.
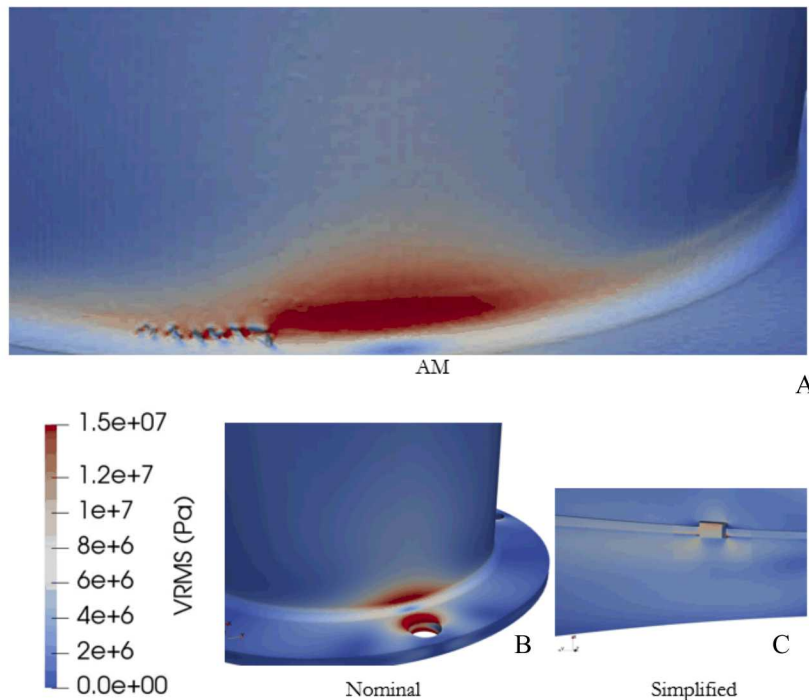

Fig. 18- 3σ VRMS Stress: Random Vibration in Z-Direction, AM (A), Nominal (B), and Simplfied Close-Up (C)

CONCLUSION

This work demonstrates that the presence of AM defects can influence the structural characteristics of a component, and that a high-fidelity model can be used to account for these effects. CT scan data of an as-built AM part was directly incorporated into an FE model and structural analysis was performed to investigate the impact of defects such as porosity, voids, and geometric distortion. These defects produced differences in frequency, mode shape, acceleration, and stress as compared to the nominal part. Utilizing a high-fidelity model to evaluate structural response of an AM component can help improve the accuracy of dynamic characterization and failure assessment of a part with defects.

Future work will investigate using modal test data for validation, which will increase confidence in the AM model and its predictive capability. In addition, an improved algorithm for representing simplified defects could be beneficial, as results of the study showed that only looking at surface defects is not effective. Efforts to improve the model will also consider other factors such as anisotropic AM properties and increased refinement at local defects.

REFERENCES

[1] B. Barroqueiro, A. Andrade-Campos, R. A. F. Valente, and V. Neto, "Metal Additive Manufacturing Cycle in Aerospace Industry: A Comprehensive Review," *Journal of Manufacturing and Materials Processing*, vol. 3, issue 3. Jun. 2019.

[2] A. Thompson, I. Maskery, and R. K. Leach, "X-ray computed tomography for additive manufacturing: a review," *Measurement Science and Technology*, vol. 27. Jun. 2016.

[3] F. Esposito, A. Gatto, E. Bassoli, and L. Denti," A Study on the Use of XCT and FEA to Predict the Elastic Behavior of Additively Manufactured Parts of Cylindrical Geometry," *Journal of Nondestructive Evaluation,* vol. 37, no. 72 Sept. 2018.

[4] H. Taheri, M. R. B. M. Shoaib, L. W. Koester, T. A. Bigelow, P. C. Collins, and L. J. Bond. "Powder-based additive manufacturing-a review of types of defects, generation mechanisms, detection, property evaluation and metrology." International Journal of Additive and Subtractive Materials Manufacturing, vol. 1, no. 2, pp. 172-209. 2017.

[5] Sandia National Laboratories, "Sierra Structural Dynamics - Users Notes 4.50.". United States. 2018. doi:10.2172/1474020.

APPENDIX

Table A 1- Natural Frequency comparison

Mode	Nominal Frequency (Hz)	AM Frequency (Hz)	% Diff. from Nominal	Simple Defect Frequency (Hz)	% Diff. from Nominal	% Diff. from AM
1	730.3	681.4	-6.7	737.0	0.9	8.2
2	1149.2	1139.7	-0.8	1150.4	0.1	0.9
3	1149.2	1151.0	0.2	1150.9	0.1	0.0
4	1566.9	1406.4	-10.2	1596.8	1.9	13.5
5	1984.8	2031.5	2.4	1984.7	0.0	-2.3
6	2011.9	2060.0	2.4	2012.0	0.0	-2.3
7	2696.7	2450.5	-9.1	2754.2	2.1	12.4
8	2696.7	2531.1	-6.1	2760.8	2.4	9.1
9	3162.8	3227.4	2.0	3165.0	0.1	-1.9
10	3162.9	3233.5	2.2	3165.1	0.1	-2.1
11	3907.9	3806.0	-2.6	3949.9	1.1	3.8
12	4355.7	4195.9	-3.7	4354.4	0.0	3.8
13	4521.9	4352.8	-3.7	4523.9	0.0	3.9
14	4522.0	4357.3	-3.6	4525.5	0.1	3.9
15	4570.1	4565.5	-0.1	4570.2	0.0	0.1
16	4571.2	4575.7	0.1	4571.2	0.0	-0.1
17	5058.3	4827.1	-4.6	5155.7	1.9	6.8
18	5171.1	4949.6	-4.3	5245.9	1.4	6.0
19	5171.1	4966.2	-4.0	5265.0	1.8	6.0
20	5288.7	5062.4	-4.3	5415.0	2.4	7.0
21	5519.5	5397.5	-2.2	5519.2	0.0	2.3
22	5571.9	5431.2	-2.5	5631.7	1.1	3.7
23	5806.5	5525.4	-4.8	5901.1	1.6	6.8
24	5806.7	5541.6	-4.6	5919.7	1.9	6.8
25	6201.1	5796.4	-6.5	6251.9	0.8	7.9
26	6252.0	6089.0	-2.6	6252.0	0.0	2.7
27	6252.0	6090.4	-2.6	6435.7	2.9	5.7
28	7030.4	6961.2	-1.0	7029.7	0.0	1.0
29	7030.4	6962.9	-1.0	7030.0	0.0	1.0
30	7850.5	7589.5	-3.3	7855.3	0.1	3.5

Table A 2- All shock results summary

Value	Nominal	AM	Simplified
Peak Acceleration X (G)	190.3	192.1	188.9
Peak Shock Response X (G)	491.5	498.6	454.9
Peak Acceleration Y (G)	247.5	234.2	246.9
Peak Shock Response Y (G)	898.7	868.4	897.5
Peak Acceleration Z (G)	252.2	261.4	251.0
Peak Shock Response Z (G)	910.7	937.5	908.1

Table A 3- All vibration results summary

Value	Nominal	AM	Simplified
Peak Response X (G^2/Hz)	111.5	133.4	217.3
Max GRMS X (G)	281.3	268.1	312.4
Peak Response Y (G^2/Hz)	110.9	112.6	104.2
Max GRMS Y (G)	150.0	139.3	152.0
Peak Response Z (G^2/Hz)	111.4	127.8	104.5
Max GRMS Z (G)	152.1	152.4	154.4